Inverse cascade from helical and nonhelical decaying columnar magnetic fields

Axel Brandenburg[1,2,3,4]†, Longqing Yi[5,6]‡ and Xianshu Wu[5]

[1]Nordita, KTH Royal Institute of Technology and Stockholm University, Hannes Alfvéns väg 12, SE-10691 Stockholm, Sweden

[2]The Oskar Klein Centre, Department of Astronomy, Stockholm University, AlbaNova, SE-10691 Stockholm, Sweden

[3]McWilliams Center for Cosmology & Department of Physics, Carnegie Mellon University, Pittsburgh, PA 15213, USA

[4]School of Natural Sciences and Medicine, Ilia State University, 3-5 Cholokashvili Avenue, 0194 Tbilisi, Georgia

[5]Tsung-Dao Lee Institute, Shanghai Jiao Tong University, Shanghai 201210, China

[6]School of Physics and Astronomy, Shanghai Jiao Tong University, Shanghai 200240, China

Powerful lasers may in future produce magnetic fields that would allow us to study turbulent magnetohydrodynamic inverse cascade behavior. This has so far only been seen in numerical simulations. In the laboratory, however, the produced fields may be highly anisotropic. Here, we present corresponding simulations to show that, during the turbulent decay, such a magnetic field undergoes spontaneous isotropization. As a consequence, we find the decay dynamics to be similar to that in isotropic turbulence. We also find that an initially pointwise nonhelical magnetic field is unstable and develops magnetic helicity fluctuations that can be quantified by the Hosking integral. It is a conserved quantity that characterizes magnetic helicity fluctuations and governs the turbulent decay when the mean magnetic helicity vanishes. As in earlier work, the ratio of the magnetic decay time to the Alfvén time is found to be around 50 in the helical and nonhelical cases. At intermediate times, the ratio can even reach a hundred. This ratio determines the endpoints of cosmological magnetic field evolution.

1. Introduction

In the absence of any initial velocity field and without any type of forcing, an initially random magnetic field can only decay. This decay can be sped up by turbulent gas motions driven through the Lorentz force that is being exerted by the magnetic field itself. The decay of such a random field obeys powerlaw behavior where the magnetic energy density $\mathcal{E}_{\mathrm{M}}$ decays with time t like $\mathcal{E}_{\mathrm{M}}(t) \propto t^{-p}$, and the magnetic correlation length ξ_{M} increases like $\xi_{\mathrm{M}} \propto t^q$. For a helical magnetic field, we have $p = q = 2/3$ (Hatori 1984; Biskamp & Müller 1999), while for a nonhelical magnetic field, we have $p = 10/9$ and $q = 4/9$ (Hosking & Schekochihin 2021; Zhou *et al.* 2022). Such a decay has been seen in many hydromagnetic numerical simulations (Brandenburg *et al.* 2015; Hosking & Schekochihin 2021; Armua *et al.* 2023; Brandenburg *et al.* 2023), but not yet in plasma experiments. With the advance of high-powered lasers it is already possible to produce magnetic fields in the laboratory (Tzeferacos *et al.* 2018), and similar advances

---

† Email address for correspondence: brandenb@nordita.org
‡ Email address for correspondence: lqyi@sjtu.edu.cn

may also allow us to achieve sufficient scale separation to perform meaningful inverse cascade experiments. However, such magnetic fields may be strongly anisotropic, so the question arises to what extent this affects the otherwise familiar decay dynamics.

Our goal here is to study the decay of an array of magnetic flux tubes with an electric current that is aligned with the magnetic field (Jiang *et al.* 2021). Such a field is indeed highly anisotropic such that the correlation length in the direction along the tubes is much larger than that perpendicular to it. A simple numerical realization of such a magnetic field is what is called the Roberts field I, which is more commonly also known as Roberts flow I. It is one of four flow fields studied by Roberts (1972) in the context of dynamo theory. The field is fully helical, but with a slight modification, it can become a pointwise nonhelical field, which is then called the Roberts field II. Both fields are here of interest. They are defined in section 2, along with a proper measure of anisotropy, the relevant evolution equations, and relevant input and output parameters. In section 3, we present numerical results for both flows using different magnetic diffusivities and scale separation ratios. Inverse cascading during the turbulent decay of helical and nonhelical magnetic fields has applications to primordial magnetic fields in the radiation dominated era of the Universe, which are discussed in section 4. We conclude in section 5.

2. Our model

2.1. *Roberts fields*

To fix our geometry, we assume magnetic flux tubes to extend in the z direction and being perpendicular to the xy plane. Such a field can be realized by the so-called Roberts field I, i.e., the magnetic field $\boldsymbol{B}$ is given by

$$\boldsymbol{B} = \boldsymbol{B}_\mathrm{I} \equiv \boldsymbol{\nabla} \times \phi\hat{\boldsymbol{z}} + \sqrt{2}k_0\phi\hat{\boldsymbol{z}}, \quad \text{where} \quad \phi = k_0^{-1}B_0 \sin k_0x \sin k_0y. \qquad (2.1)$$

is an xy periodic field. Such a magnetic field has a component in the z direction, but no variation along that direction, so it is highly anisotropic. This may change with time as the magnetic field undergoes a turbulent decay. The Roberts field I is maximally helical with $\boldsymbol{A} \cdot \boldsymbol{B} = \sqrt{2}k_0^{-1}B_0^2(\sin^2 k_0x + \sin^2 k_0y)$, so $\langle \boldsymbol{A} \cdot \boldsymbol{B} \rangle = \sqrt{2}k_0^{-1}B_0^2$. Here, $\boldsymbol{A}$ is the magnetic vector potential and $\boldsymbol{B} = \boldsymbol{\nabla} \times \boldsymbol{A}$. The Roberts field II, by contrast, is given by

$$\boldsymbol{B} = \boldsymbol{B}_\mathrm{II} \equiv \boldsymbol{\nabla} \times \phi\hat{\boldsymbol{z}} + k_\mathrm{f}\tilde{\phi}\hat{\boldsymbol{z}}, \quad \text{where} \quad \tilde{\phi} = k_0^{-1}B_0 \cos k_0x \cos k_0y, \qquad (2.2)$$

where $\tilde{\phi}$ is 90° phase shifted in the x and y directions relative to $\phi(x, y)$ and $k_\mathrm{f} = \sqrt{2}k_0$ is the eigenvalue of the curl operator for field I, i.e., $\boldsymbol{\nabla} \times \boldsymbol{B}_\mathrm{I} = k_\mathrm{f}\boldsymbol{B}_\mathrm{I}$, so $\boldsymbol{B}_\mathrm{I} \cdot \boldsymbol{\nabla} \times \boldsymbol{B}_\mathrm{I} = k_\mathrm{f}\boldsymbol{B}_\mathrm{I}^2$, while $\boldsymbol{B}_\mathrm{II} \cdot \boldsymbol{\nabla} \times \boldsymbol{B}_\mathrm{II} = 0$ pointwise. Both for fields I and II, we have $\langle \boldsymbol{B}^2 \rangle = 2B_0^2$.

2.2. *Quantifying the emerging anisotropy*

To quantify the degree of anisotropy, we must separate the derivatives of the magnetic field along the z direction ($\boldsymbol{\nabla}_\parallel$) from those perpendicular to it ($\boldsymbol{\nabla}_\perp$), so $\boldsymbol{\nabla} = \boldsymbol{\nabla}_\parallel + \boldsymbol{\nabla}_\perp$. We also decompose the magnetic field analogously, i.e., $\boldsymbol{B} = \boldsymbol{B}_\parallel + \boldsymbol{B}_\perp$. The mean current density can be decomposed similarly, i,e., $\boldsymbol{J} = \boldsymbol{J}_\parallel + \boldsymbol{J}_\perp$, but this decomposition mixes the underlying derivatives. We see this by computing $\boldsymbol{J} \equiv \boldsymbol{\nabla} \times \boldsymbol{B}$ (where the permeability has been set to unity). Using this decomposition, we find

$$\boldsymbol{J} = \boldsymbol{\nabla}_\parallel \times \boldsymbol{B}_\perp + \boldsymbol{\nabla}_\perp \times \boldsymbol{B}_\parallel + \boldsymbol{\nabla}_\perp \times \boldsymbol{B}_\perp, \qquad (2.3)$$

noting that $\boldsymbol{\nabla}_\parallel \times \boldsymbol{B}_\parallel = 0$. The term of interest for characterizing the emergent isotropization is the first one, $\boldsymbol{\nabla}_\parallel \times \boldsymbol{B}_\perp$, because it involves only parallel derivatives (z derivatives), which vanish initially. We monitor the ratio of its mean squared value to $\langle \boldsymbol{J}^2 \rangle$.

The last term in equation (2.3) is just $\boldsymbol{J}_\parallel = \boldsymbol{\nabla}_\perp \times \boldsymbol{B}_\perp$, but the first and second terms cannot simply be expressed in terms of $\boldsymbol{J}_\perp$, although $\boldsymbol{\nabla}_\parallel \times \boldsymbol{B}_\perp$ would be $\boldsymbol{J}_\perp$ if the magnetic field only had a component in the plane, and $\boldsymbol{\nabla}_\perp \times \boldsymbol{B}_\parallel$ would be $\boldsymbol{J}_\perp$ if the magnetic field only had a component out of the plane. We therefore denote those two contributions in the following by $\boldsymbol{J}_{\perp\perp}$ and $\boldsymbol{J}_{\perp\parallel}$, respectively, so that $\boldsymbol{J}_{\perp\perp} + \boldsymbol{J}_{\perp\parallel} = \boldsymbol{J}_\perp$.

Thus, as motivated above, to monitor the emergent isotropization, we determine $\langle \boldsymbol{J}_{\perp\perp}^2 \rangle / \langle \boldsymbol{J}^2 \rangle$. For isotropic turbulence, we find that this ratio is about $4/15 \approx 0.27$, and this is also true for $\langle \boldsymbol{J}_{\perp\parallel}^2 \rangle / \langle \boldsymbol{J}^2 \rangle$; see Appendix A for an empirical demonstration. In the expression for $\langle \boldsymbol{J}^2 \rangle$, there is also a mixed term, $\boldsymbol{J}_{\perp\mathrm{m}}^2 = -2\langle B_{x,z}B_{z,x} + B_{y,z}B_{z,y}\rangle$, which turns out to be positive in practice. Here, commas denote partial differentiation. Thus, we have

$$\langle \boldsymbol{J}^2 \rangle = \langle \boldsymbol{J}_{\perp\perp}^2 \rangle + \langle \boldsymbol{J}_{\perp\parallel}^2 \rangle + \langle \boldsymbol{J}_{\perp\mathrm{m}}^2 \rangle + \langle \boldsymbol{J}_\parallel^2 \rangle. \tag{2.4}$$

In the isotropic case, we find $\langle \boldsymbol{J}_\parallel^2 \rangle / \langle \boldsymbol{J}^2 \rangle = 1/3$, and for the mixed term we then have $\langle \boldsymbol{J}_{\perp\mathrm{m}}^2 \rangle / \langle \boldsymbol{J}^2 \rangle = 2/15 \approx 0.13$.

2.3. Evolution equations

To study the decay of the magnetic field, we solve the evolution equations of magneto-hydrodynamics (MHD) for an isotropic compressible gas with constant sound speed c_s, so the gas density ρ is proportional to the pressure $p = \rho c_\mathrm{s}^2$. In that case, $\ln \rho$ and the velocity $\boldsymbol{u}$ obey

$$\frac{\mathrm{D}\ln\rho}{\mathrm{D}t} = -\boldsymbol{\nabla} \cdot \boldsymbol{u}, \tag{2.5}$$

$$\frac{\mathrm{D}\boldsymbol{u}}{\mathrm{D}t} = -c_\mathrm{s}^2 \boldsymbol{\nabla}\ln\rho + \frac{1}{\rho}\left[\boldsymbol{J} \times \boldsymbol{B} + \boldsymbol{\nabla} \cdot (2\rho\nu\mathsf{S})\right], \tag{2.6}$$

where $\mathrm{D}/\mathrm{D}t = \partial/\partial t + \boldsymbol{u} \cdot \boldsymbol{\nabla}$ is the advective derivative, ν is the kinematic viscosity, S is the rate-of-strain tensor with components $\mathsf{S}_{ij} = (u_{i,j} + u_{j,i})/2 - \delta_{ij}\boldsymbol{\nabla} \cdot \boldsymbol{u}/3$, and α is the photon drag coefficient (Banerjee & Jedamzik 2004), which is included in some of our simulations. To ensure that the condition $\boldsymbol{\nabla} \cdot \boldsymbol{B} = 0$ is obeyed at all times, we also solve the uncurled induction equation for $\boldsymbol{A}$, i.e.,

$$\frac{\partial \boldsymbol{A}}{\partial t} = \boldsymbol{u} \times \boldsymbol{B} - \eta\boldsymbol{J}. \tag{2.7}$$

As before, the permeability is set to unity, so $\boldsymbol{J} = \boldsymbol{\nabla} \times \boldsymbol{B}$ is the current density.

We use the PENCIL CODE (Pencil Code Collaboration *et al.* 2021), which is well suited for our MHD simulations. It uses sixth order accurate spatial discretizations and a third order time-stepping scheme. We adopt periodic boundary conditions in all three directions, so the mass is conserved and the mean density is $\langle \rho \rangle \equiv \rho_0$ is constant. The size of the domain is $L_\perp \times L_\perp \times L_\parallel$ and the lowest wavenumber in the plane is $k_1 = 2\pi/L_\perp$. By default, we choose $\rho_0 = k_1 = c_\mathrm{s} = \mu_0 = 1$ which fixes all dimensions in the code.

2.4. Input and output parameters

In the following, we study cases with different values of k_0. We specify the amplitude of the vector potential to be $A_0 = 0.02$ for most of the runs with Roberts field I and $A_0 = 0.05$ for Roberts field II. We use $k_0 = 16$, so $B_0 = k_0 A_0 = 0.32$ for field I and 0.8 for field II. For other values of k_0, we adjust A_0 such that B_0 is unchanged in all cases. This implies $\langle \boldsymbol{B}^2 \rangle = 2B_0^2 = 0.2$ and 1.28, and therefore $B_\mathrm{rms} = 0.45$ and 1.13, respectively. The initial values of the Alfvén speed, $v_{\mathrm{A}0} = B_\mathrm{rms}/\sqrt{\mu_0\rho_0}$, are therefore transonic. We often give the time in code units, $(c_\mathrm{s}k_1)^{-1}$, but sometimes we also give it in units of

$(v_{A0}k_0)^{-1}$, which is physically more meaningful. However, we must remember that the actual magnetic field and therefore the actual Alfvén speed are of course decaying.

In addition to the Roberts field, we add to the initial condition Gaussian-distributed noise of a relative amplitude of 10^{-6}. This allows us to study the stability of the field to small perturbations. To measure the growth rate, we compute the semilogarithmic derivative of $\langle \boldsymbol{J}_{\perp\perp}^2 \rangle / \langle \boldsymbol{J}^2 \rangle$ for a suitable time interval.

The number of eddies in the plane is characterized by the ratio k/k_1. The aspect ratio of the domain is quantified by $L_\parallel/L_\perp$. The electric conductivity is quantified by the Lundquist number $\mathrm{Lu} = v_{A0}/\eta k_0$, and the kinematic viscosity is related to η through the magnetic Prandtl number, $\mathrm{Pr_M} = \nu/\eta$. In all our cases, we keep $\mathrm{Pr_M} = 5$. For most of our runs, we use $\eta \times 10^{-7} c_s/k_1$ in code units.

Important output parameters are the growth rate $\lambda = \mathrm{d}\ln(\langle \boldsymbol{J}_{\perp\perp}^2 \rangle / \langle \boldsymbol{J}^2 \rangle)/\mathrm{d}t$, evaluated in the regime where it is approximately constant. It is made nondimensional through the combination $\lambda/v_{A0}k_0$. We also present magnetic energy and magnetic helicity variance spectra, $\mathrm{Sp}(\boldsymbol{B})$ and $\mathrm{Sp}(h)$, respectively. These spectra also depend on k and t, so we denote the spectra sometimes also as $\mathrm{Sp}(\boldsymbol{B}; k, t)$ and $\mathrm{Sp}(h; k, t)$, respectively.

Since $\rho \approx \rho_0 = 1$, the value of B_rms is also equal to the instantaneous Alfvén speed, v_A, and its square is the mean magnetic energy density, $\mathcal{E}_M = \langle \boldsymbol{B}^2 \rangle / 2$. The latter can also be computed from the magnetic energy spectrum $E_M(k, t) = \mathrm{Sp}(\boldsymbol{B})$ through $\mathcal{E}_M = \int E_M(k, t)\,\mathrm{d}k$. The integral scale of the magnetic field is given by

$$\xi_M(t) = \int k^{-1} E_M(k, t)\,\mathrm{d}k / \mathcal{E}_M. \tag{2.8}$$

It is also of interest to compare its evolution with the magnetic Taylor microscale, $\xi_T = B_\mathrm{rms}/J_\mathrm{rms}$, where J_rms is the root-mean-squared current density, i.e., $(\boldsymbol{\nabla} \times \boldsymbol{B})_\mathrm{rms}$. (We recall that the permeability was set to unity; otherwise, there would have been an extra μ_0 factor in front of J_rms.) Both in experiments and in simulations, ξ_T may be more easily accessible than ξ_M, so it is important to find out whether the two obey similar scaling relations.

During the decay, $\mathcal{E}_M = v_A^2/2$ decreases and ξ_M increases. The Alfvén time, i.e., the ratio $\tau_A \equiv \xi_M/v_A$, therefore also increases; see Banerjee & Jedamzik (2004) and Hosking & Schekochihin (2023) for early considerations of this point. Both for standard (isotropic) helical decay with $v_A \propto t^{-1/3}$ and $\xi_M \propto t^{2/3}$, as well as for nonhelical decay with $v_A \propto t^{-5/9}$ and $\xi_M \propto t^{4/9}$, the value of τ_A increases linearly with t, i.e.,

$$t \propto \tau_A(t). \tag{2.9}$$

This is also consistent with the idea that the turbulent decay is self-similar (Brandenburg & Kahniashvili 2017). It was found that the ratio $t/\tau_A(t)$ approaches a constant that increases with the Lundquist number (Brandenburg *et al.* 2024). The difference between the quantity $t/\tau_A(t)$ and the factor C_M defined in Brandenburg *et al.* (2024) is the exponent $p = 10/9$ in the relation $\mathcal{E}_M \propto t^{-p}$ for nonhelical and $p = 2/3$ for helical turbulence with $t/\tau_A = C_M/p$.

To compute the Hosking integral, we need the function $\mathcal{I}_H(R, t)$, which is a weighted integral over $\mathrm{Sp}(h)$, given by

$$\mathcal{I}_H(R, t) = \int_0^\infty w(k, R)\,\mathrm{Sp}(h; k, t)\,\mathrm{d}k, \quad \text{where} \quad w(k, R) = \frac{4\pi R^3}{3}\left[\frac{6j_1(kR)}{kR}\right]^2, \tag{2.10}$$

and $j_1(x) = (\sin x - x\cos x)/x^2$ is the spherical Bessel function of order one. As shown by Zhou *et al.* (2022), the function $\mathcal{I}_H(R, t)$ yields the Hosking integral in the limit of
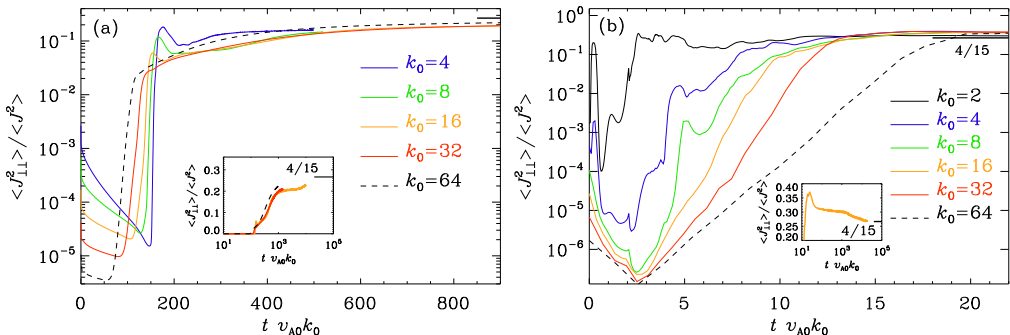
FIGURE 1. Evolution of $\langle \boldsymbol{J}_{\perp\perp}^2 \rangle / \langle \boldsymbol{J}^2 \rangle$ for (a) Roberts field I with $k_0 = 4$ (blue), 8 (green), 16 (orange), 32 (red), and 64 (black dashed), and for (b) Roberts field II with $k_0 = 2$ (black), 4 (blue), 8 (green), 16 (orange), 32 (red), and 64 (black dashed). The short thick line on the upper right indicates the value of $4/15$, which is reached only at much later times outside this plot. The insets demonstrates that $\langle \boldsymbol{J}_{\perp\perp}^2 \rangle / \langle \boldsymbol{J}^2 \rangle \to 4/15$ much later.

large radii R, although R must still be small compared with the size of the domain. They referred to this as the box-counting method for a spherical volume with radius R.

3. Results

3.1. *Isotropization*

In figure 1, we show the evolution of $\langle \boldsymbol{J}_{\perp\perp}^2 \rangle / \langle \boldsymbol{J}^2 \rangle$ for Roberts fields I and II. We see that, after a short decay phase, exponential growth commences followed by a saturation of this ratio. We expect the ratio $\langle \boldsymbol{J}_{\perp\perp}^2 \rangle / \langle \boldsymbol{J}^2 \rangle$ to reach the value $4/15$ at late times; see Appendix A. The insets of figure 1 show the degree to which this is achieved at late times. Especially in the helical case, when inverse cascading is strong, the peak of the spectrum has already reached the lowest wavenumber of the domain. This is probably the reason why the value of $4/15$ has not been reached by the end of the simulation.

The early growth of $\langle \boldsymbol{J}_{\perp\perp}^2 \rangle / \langle \boldsymbol{J}^2 \rangle$ shows that both the Roberts fields I and II are unstable to perturbations and develop an approximately isotropic state. The normalized growth rates are given in table 1 along with the times $t_{\rm p}$ of maximum growth. The normalized values are in the range 0.7 to 6, but mostly around unity for intermediate values around $k_0 = 16$. The normalized times, $t_{\rm p} v_{\rm A0} k_0$, tend to decrease with increasing values of k_0 and are about ten to twenty times larger for field I than for field II. This difference was also found in another set of simulations in which B_0 was the same for fields I and II; see Appendix B.

Visualizations of B_z on the periphery of the computational domain are shown in figure 2 for Roberts fields I and II. The initially tube-like structures are seen to decay much faster for Roberts field II. At time $t = 100$, the magnetic field has much larger structures for Roberts field I than at time $t = 1000$ for Roberts field II.

3.2. *Spectral evolution*

In figure 3, we plot magnetic energy and magnetic helicity variance spectra for the Roberts field I. Note that the spectra are normalized by $v_{\rm A}^2 k_0^{-1}$ and $v_{\rm A}^4 k_0^{-3}$, respectively. At early times, the spectra show spikes at $k \approx k_{\rm f}$ and $2k_0$, respectively, along with higher harmonics. We also show the time evolution of the normalized values of these spectra at the lowest wavenumber $k = k_1$. For $\mathrm{Sp}(h)$, we also scale by $2\pi^2/k^2$, which then gives

TABLE 1. Normalized growth rates λ and peak times t_p for different values of k_0/k_1. The hyphen indicates that no growth occurred.

field	$k_0 =$	2	4	8	16	32	64
I	$\lambda/v_\mathrm{A0}k_0 =$	—	2.9	1.4	1.1	0.7	0.5
II	$\lambda/v_\mathrm{A0}k_0 =$	5.5	1.2	0.8	1.9	1.6	1.0
I	$t_\mathrm{p}v_\mathrm{A0}k_0 =$	—	34	16	7.7	3.4	1.2
II	$t_\mathrm{p}v_\mathrm{A0}k_0 =$	1.0	1.6	2.0	0.3	0.2	0.1
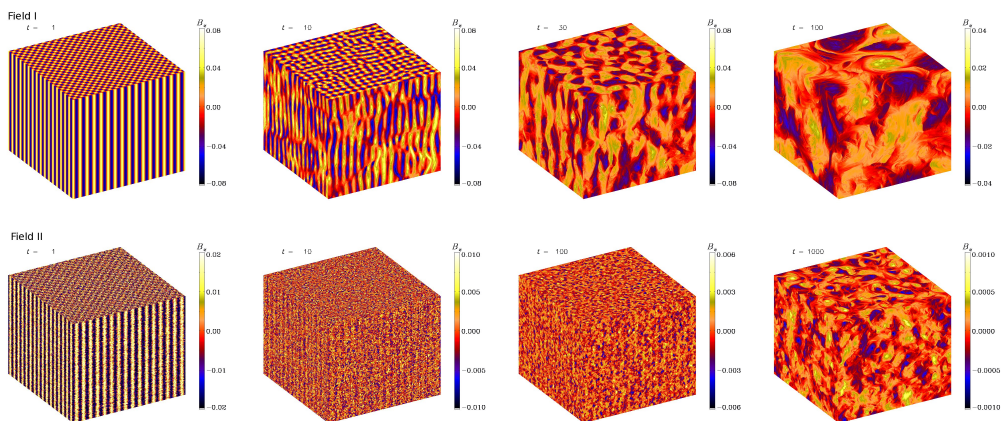
FIGURE 2. Visualizations of B_z on the periphery of the computational domain at times $t = 1$, 10, 30, and 100 for Roberts field I (top) and at times $t = 1$, 10, 100, and 1000 for Roberts field II (bottom).

an approximation to the value of the Hosking integral (Hosking & Schekochihin 2021). Again, we see a sharp rise in both time series when the fields becomes unstable.

We also see that at late times, a bump appears in the spectrum near the Nyquist wavenumber. This shows that the Lundquist number was somewhat too large for the resolution of 1024^3. However, comparing with simulations at lower Lundquist numbers shows that the large-scale evolution has not been adversely affected by this.

In figure 4, we show the same spectra for the case of Roberts fields II. Again, we see spikes in the spectra at early times. Those of $\mathrm{Sp}(\boldsymbol{B})$ are again at $\sqrt{2}k_0$, along with overtones, but those of $\mathrm{Sp}(h)$ are now at $2\sqrt{2}k_0$ instead of $2\,k_0$, and there are no spikes of $\mathrm{Sp}(h)$ at $t = 0$. This is a consequence of the fact that the field has zero initial helicity pointwise, and helicity is quickly being produced owing to the growth of the initial perturbations. The plot of $\mathrm{Sp}(h; k_1, t)$ shows nearly perfectly a constant level for $tv_\mathrm{A}k_0 = 100$. This indicates that the Hosking integral is well conserved by that time.

3.3. *Spontaneous production of magnetic helicity variance*

As we have seen from figure 4, the case of zero magnetic helicity variance is unstable and there is a rapid growth of $\mathrm{Sp}(h)$ also at small wavenumbers. This was already anticipated
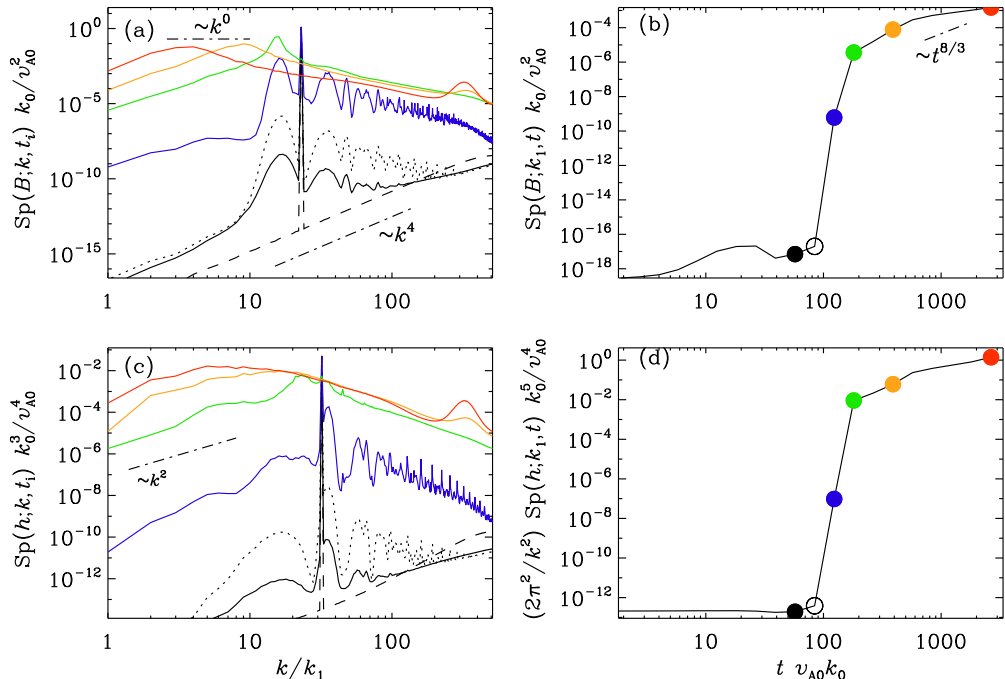
FIGURE 3. Evolution of magnetic energy and magnetic helicity variance spectra, $\mathrm{Sp}(\boldsymbol{B})$ and $\mathrm{Sp}(h)$, respectively, for Roberts field I with $k_0 = 16$ at different times t_i indicated by different colors and line types as seen in the time traces on the right. The open black symbols in panels (b) and (d) correspond to the dotted lines in panels (a) and (c).

by Hosking & Schekochihin (2021), and the present experiments with the Roberts field II show this explicitly.

We now discuss the function $\mathcal{I}_{\mathrm{H}}(R,t)$; see Hosking & Schekochihin (2021) and Zhou *et al.* (2022). The result is shown in figure 5. For small values of R, $\mathcal{I}_{\mathrm{H}}(R)$ increases $\propto R^3$. This indicates that the mean squared magnetic helicity density is not randomly distributed on those scales. In the present case, the actual scaling is slightly shallower than R^3, which is probably due to the finite scale separation. For $R \approx 1$, corresponding to scales compatible to the size of the computational domain, we see that $\mathcal{I}_{\mathrm{H}}(R)$ has a plateau. It is at those scales, $R = R_*$, that we must determine the Hosking integral $I_{\mathrm{H}}(t) = \mathcal{I}_{\mathrm{H}}(t, R_*)$. In figure 6, we show the time dependence of $I_{\mathrm{H}}(t)$ for Roberts field II with $k_0 = 16$ normalized both by $v_{\mathrm{A}0}^4/k_0^5$ (which is constant) and by $\mathcal{E}_{\mathrm{M}}^2\xi_{\mathrm{M}}^5$ (which is time-dependent). Note that the time axis is here also logarithmic. We see an early rapid growth of $I_{\mathrm{H}}(t)$ over eight orders of magnitude.

Previous work showed that the value of $I_{\mathrm{H}}(t)$ can greatly exceed the dimensional estimate $\mathcal{E}_{\mathrm{M}}^2\xi_{\mathrm{M}}^5$ (Zhou *et al.* 2022). Figure 6 shows that at late times, $tv_{\mathrm{A}0}k_0 > 100$, this is also the case here. After the initial rapid growth phase, however, the normalized value of $I_{\mathrm{H}}(t)$ is still well below unity (around 0.03). The growth of $I_{\mathrm{H}}/\mathcal{E}_{\mathrm{M}}^2\xi_{\mathrm{M}}^5$ after $tv_{\mathrm{A}0}k_0 > 100$ is mostly due to the decay of $\mathcal{E}_{\mathrm{M}}$ and it is later counteracted by a growth of ξ_{M}. The dashed blue and orange lines in figure 6(a) show separately the evolutions for $\mathcal{E}_{\mathrm{M}}^2/v_{\mathrm{A}0}^4$ and $\xi_{\mathrm{M}}^5 k_0^5$, respectively.

If the Hosking scaling applies to the present case of initially anisotropic MHD turbulence, we expect $\xi_{\mathrm{M}} \propto t^{4/9}$ and therefore $\xi_{\mathrm{M}}^5 \propto t^{20/9}$. The actual slope seen in figure 6 is however around 3 at late times. For $\mathcal{E}_{\mathrm{M}}$, we expect a $t^{-10/9}$ scaling and therefore
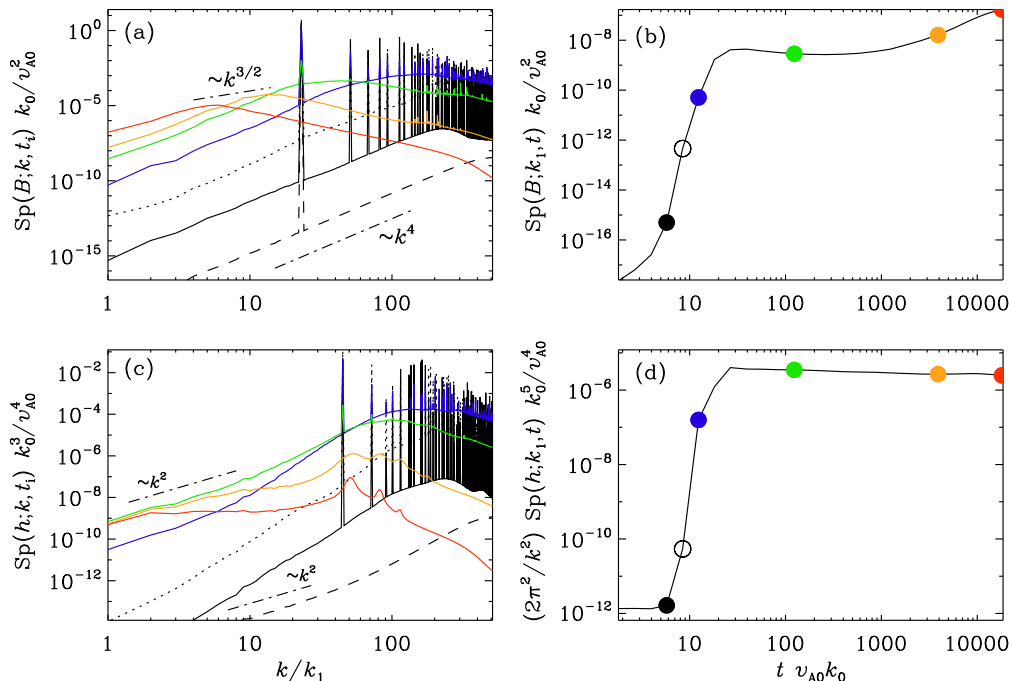
FIGURE 4. Same as figure 3, but for the Roberts field II at different times t_i as seen in the time traces on the right.
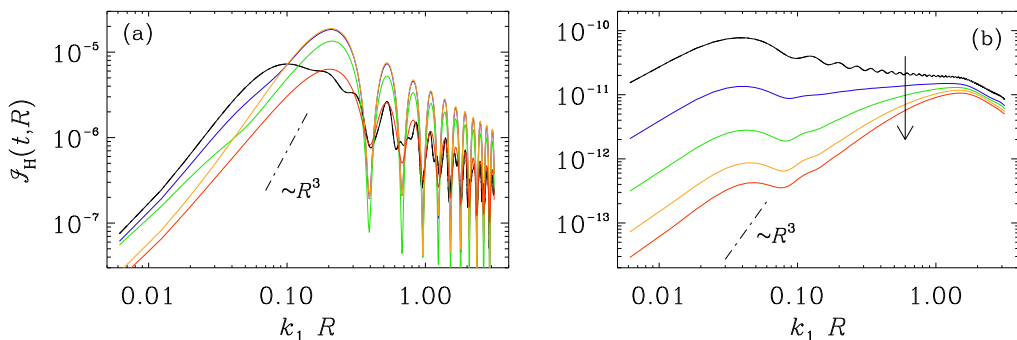

FIGURE 5. $\mathcal{I}_H(R)$ for Roberts field II with (a) $k_0 = 4$ at $t = 1$ (black), 1.5 (blue), 2.2 (green), 3.2 (orange), and 4.6 (red). and (b) $k_0 = 16$ at $t = 46$ (black), 147 (blue), 316 (green), 570 (orange), and 824 (red). The arrow indicates the sense of time.

$\mathcal{E}_M^2 \propto t^{20/9}$, i.e, the reciprocal one of ξ_M^5. Again, the numerical data suggest a larger value of around 3. In section 4.1, we analyze in more detail the anticipated scaling of $\mathcal{E}_M(t) \propto t^{-p}$ and $\xi_M \propto t^q$. We find that the two instantaneous scaling exponents p and q are indeed larger than what is expected based on the Hosking phenomenology. However, the instantaneous scaling exponents also show a clear evolution toward the expected values.

   It is interesting to observe that the evolution of I_H proceeds in two distinct phases. In the first one, when $tv_{A0}k_0 < 2$, I_H shows a rapid growth that is not exponential; see the inset of figure 6, where the growth of I_H is shown on a semilogarithmic representation. The growth is closer to that of a power law, at the approximate exponent would be
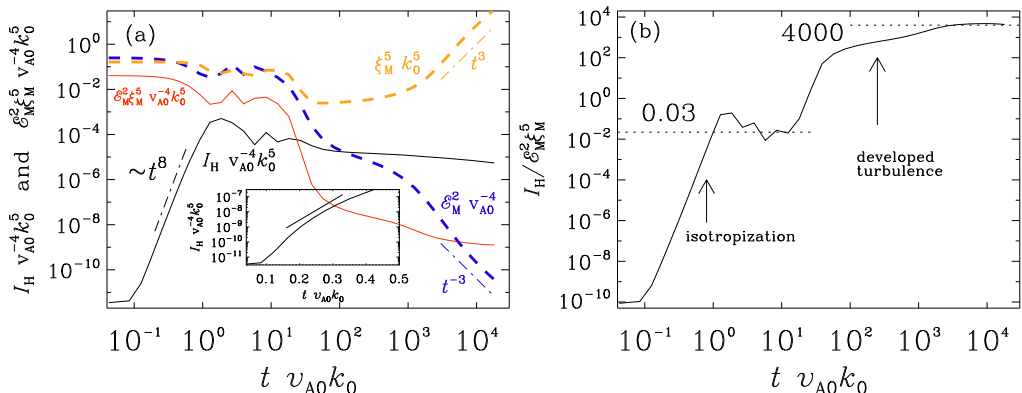
FIGURE 6. Time dependence of (a) $I_H(t)$ (black solid line) along with $\mathcal{E}_M^2 \xi_M^5$ (red solid line) in units of $v_A^4 k_0^{-5}$ as well as $\mathcal{E}_M / v_{A0}^4$ (blue dashed line) and $\xi_M^5 k_0^5$ (orange dashed line) and (b) the ratio $I_H / \mathcal{E}_M^2 \xi_M^5$ for Roberts field II with $k_0 = 16$. The plateaus at 0.03 and 3000 are marked by dotted lines. In (a), the dashed-dotted straight lines indicate the slopes $\propto t^8$ (black), $\propto t^3$ (orange), and $\propto t^{-3}$ (blue). The inset in (a) shows the growth of $I_H(t)$ in a semilogarithmic representation along with a line $\propto e^{30t}$.

around six, which is rather large. During this phase, the turbulent cascade has not yet developed, but a nonvanishing and nearly constant value of I_H has been established. However, in units of $\mathcal{E}_M^2 \xi_M^5$, its value is rather small (around 0.03).

In the second phase, when $t v_{A0} k_0 > 100$, turbulence has developed, and a turbulent decay has developed. It is during this time that the ratio $I_H(t) / \mathcal{E}_M^2 \xi_M^5$ approaches larger values (around 3000) that were previously seen in isotropic decaying turbulence simulations (Zhou et al. 2022). The reason for this large value was argued to be due to the development of non-Gaussian statistics in the magnetic field. However, Brandenburg & Banerjee (2025) presented an estimate in which the value of this ratio is equal to C_M^2. With $C_M \approx 50$, this would agree with the numerical findings.

4. Cosmological applications

4.1. Evolution in the diagnostic diagram

In view of the cosmological applications of decaying MHD turbulence, it is of interest to consider the evolution of the actual Alfvén speed $v_A(t) = \sqrt{2\mathcal{E}_M / \rho}$ in an evolutionary diagram as a parametric representation versus $\xi_M(t)$; see figure 7(a). With $v_A \propto t^{-p/2}$ and $\xi_M \propto t^q$, we expect that $v_A \propto \xi_M^{-\kappa}$ with $\kappa = p/2q = 1/2$ for the fully helical case of Roberts field I. This is in agreement with early work showing that $v_A \propto t^{1/3}$ and $\xi_M \propto t^{2/3}$ (Hatori 1984; Biskamp & Müller 1999).

In figure 7(a), we have also marked the times $t = 10$ (open symbols) and $t = 100$ (filled symbols). The points of constant times depart significantly from the lines of constant Alfvén time, τ_A, for which $v_A = \xi_M / \tau_A$ grows linearly with ξ_M. We expect the times to be larger by a factor C_M than the corresponding values of $\tau_A(t)$. This is indeed to case: the point $t = 100$ lies on the line $\tau_A = 1$, i.e., $t/\tau_A = 100$. This is twice as much as our nominal value of about 50.

There is an interesting difference between the cases of Roberts fields I and II in that for field II, there is an extended period during which ξ_M shows a rapid decrease before the expected increase emerges. The fact that such an initial decrease of the characteristic length scale is not seen for Roberts field I is remarkable. The rapid
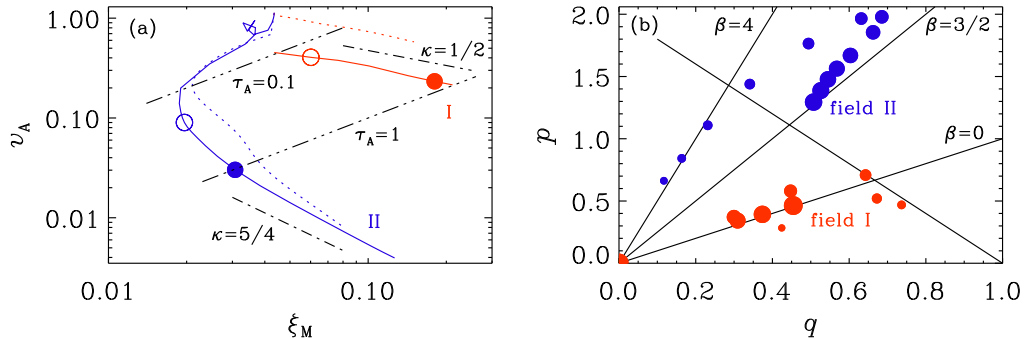
FIGURE 7. (a) Parametric representation of v_A versus ξ_M for Roberts fields I (red) and II (blue). The solid (dotted) curves are for $\eta = 2 \times 10^{-7}$ ($\eta = 4 \times 10^{-6}$). Note that the red dotted line for $\eta = 4 \times 10^{-6}$ starts at the same value $v_A = \sqrt{1.28}$ as the nonhelical runs (blue lines). The similarity between the dotted and solid red lines shows that the initial amplitude does not matter much. The open (filled) symbols indicate the times $t = 10$ ($t = 100$). The dashed-dotted lines give the slopes $\kappa = 1/2$ and $5/4$ for Roberts fields I (red) and II (blue), respectively. (b) pq diagram field fields I (red) and II (blue) with $\eta = 2 \times 10^{-7}$. Larger symbols indicate later times.
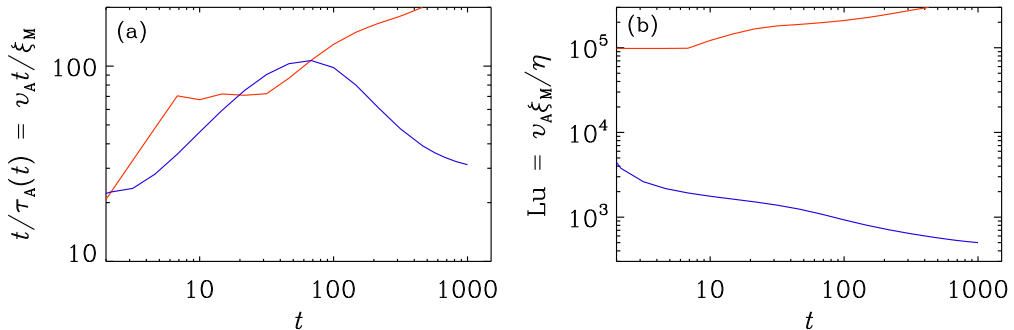

FIGURE 8. (a) t/τ_A and (b) Lu versus time for Roberts fields I (red) and II (blue).

development of smaller length scales is probably related to the breakup of the initially organized tube-like structures into smaller scales. In the helical case, however, the nonlinear interaction among helical modes can only result in the production of modes with smaller wavenumbers, i.e., larger length scales; see Frisch *et al.* (1975) and Brandenburg & Subramanian (2005) for a review. Such a constraint does not exist for the nonhelical modes, where this can then reduce the *effective* starting values of ξ_M and therefore also of the effective Alfvén time, $\tau_A = \xi_M/v_A$, early in the evolution. In Appendix B, we present similar diagrams for different values of k_0, but with a drag term included that could be motivated by cosmological applications.

We inspect the time-dependences of $t/\tau_A = v_A t/\xi_M$ and Lu $= v_A \xi_M/\eta$ for Roberts fields I and II in figure 8. We see that $t/\tau_A(t)$ reaches values in excess of 100 for $t = 100$ in both cases. This is more than what has been seen before, but it also shows significant temporal variations.

4.2. *Universality of prefactors in decay laws?*

The decay of a turbulent magnetic field is constrained by a certain conservation laws: the conservation of mean magnetic density $I_M = \langle h \rangle$, where $h = \boldsymbol{A} \cdot \boldsymbol{B}$ is the local magnetic helicity density, and the Hosking integral, $I_H = \int h(\boldsymbol{x}) h(\boldsymbol{x} + \boldsymbol{r}) \, \mathrm{d}^3 r$. When the
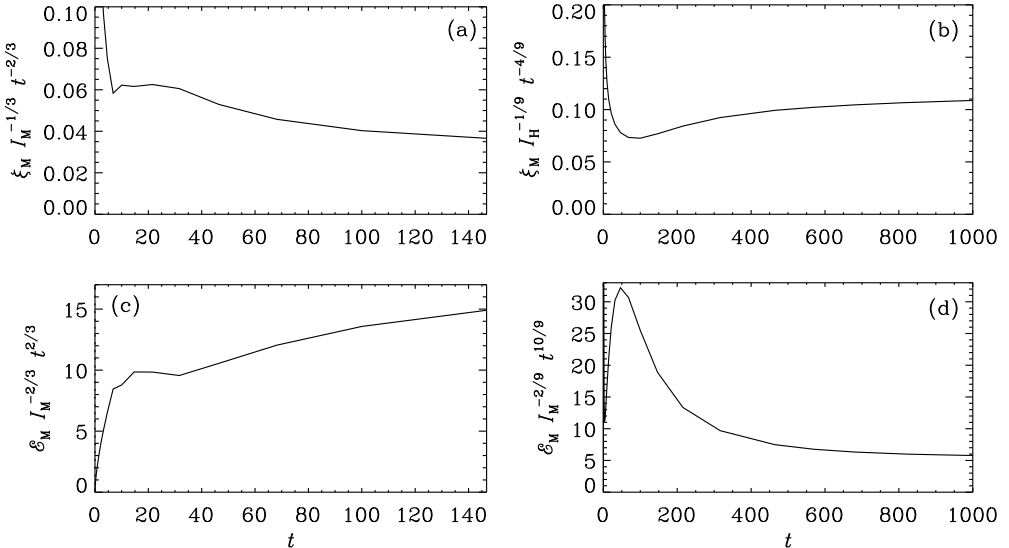
FIGURE 9. Compensated evolutions of ξ_M and $\mathcal{E}_\mathrm{M}$ allowing the nondimensional prefactors in equation (4.1) to be estimated.

TABLE 2. Summary

Reference	$C_\mathrm{M}^{(\xi)}$	$C_\mathrm{H}^{(\xi)}$	$C_\mathrm{M}^{(\mathcal{E})}$	$C_\mathrm{H}^{(\mathcal{E})}$	$C_\mathrm{M}^{(E)}$	$C_\mathrm{H}^{(E)}$
Brandenburg & Banerjee (2025)	0.12	0.14	4.3	4.0	0.7	0.025
Brandenburg et al. (2023)	—	0.12	—	3.7	—	0.025
Brandenburg & Larsson (2023)	—	0.15	—	3.8	—	0.025
present work	0.04	0.10	15	6	—	—

magnetic field is fully helical, the decay is governed by the conservation of I_M, and when it is nonhelical, it is governed by the conservation of I_H. The time of crossover depends on the ratio $t_* \equiv I_\mathrm{H}^{1/2}/I_\mathrm{M}^{3/2}$ (Brandenburg & Banerjee 2025). Specifically, the correlation length $\xi_\mathrm{M}(t)$, the mean magnetic energy $\mathcal{E}_\mathrm{M}(t)$, and the envelope of the peaks of the magnetic energy spectrum $E_\mathrm{M}(k,t)$ depends on the values of the conserved quantities with (Brandenburg & Larsson 2023)

$$\xi_\mathrm{M}(t) = C_i^{(\xi)} I_i^\sigma t^q, \quad \mathcal{E}_\mathrm{M}(t) = C_i^{(\mathcal{E})} I_i^{2\sigma} t^{-p}, \quad E_\mathrm{M}(k) \leqslant C_i^{(E)} I_i^{(3+\beta)\,q} k^\beta. \quad (4.1)$$

where σ is the exponent with which the length enters in I_i: $\sigma = 1/3$ when the mean magnetic helicity density governs the decay ($i = \mathrm{M}$) and $\sigma = 1/9$ for the Hosking integral ($i = \mathrm{H}$). In figure 9, we show the appropriately compensated evolutions of ξ_M and $\mathcal{E}_\mathrm{M}$ such that we can read off the values of $C_i^{(\xi)}$ and $C_i^{(\mathcal{E})}$ for the helical and nonhelical cases.

In table 2, we summarize the values for the six coefficients reported previously in the literature and compare with those determine here. The fact that the coefficients are now somewhat different under different circumstances suggests that they might not be universal, although the more complicated setup of the present experiment as well as limited scale separation may have contributed to their present results. This question is

significant, however, because universality would mean that the decay laws of the form (e.g., Vachaspati 2021)

$$\xi_{\mathrm{M}}(t) = \xi_{\mathrm{M}}(t_0) \, (t/t_0)^q, \quad \mathcal{E}_{\mathrm{M}}(t) = \mathcal{E}_{\mathrm{M}}(t_0) \, (t/t_0)^{-p} \tag{4.2}$$

could be misleading in that they suggest some freedom in the choice of the values of $\xi_{\mathrm{M}}(t_0)$ and $\mathcal{E}_{\mathrm{M}}(t_0)$ at the time t_0. Comparing with equation (4.1), we see that

$$\xi_{\mathrm{M}}(t_0)/t_0^q = C_i^{(\xi)} I_i^{\sigma}, \quad \text{and} \quad \mathcal{E}_{\mathrm{M}}(t_0) \, t_0^p = C_i^{(\mathcal{E})} I_i^{2\sigma}, \tag{4.3}$$

so they cannot be chosen arbitrarily, but they must obey a constraint that depends on the relevant conservation law.

5. Conclusions

We have seen that a tube-like arrangement of an initial magnetic field becomes unstable to small perturbations. The resulting magnetic field becomes turbulent and tends to isotropize over time. This means that tube-like initial conditions that could be expected in plasma experiments would allow us to study the turbulent MHD decay dynamics – even for moderate but finite scale separation of 4:1 or more. In other words, the number of tubes per side length should be at least four.

We have also seen that a pointwise nonhelical magnetic field, as in the case of the Roberts field II, is unstable and develops magnetic helicity fluctuations. After about one Alfvén time, the Hosking integral reaches a finite value, but a fully turbulent decay commences only after about one hundred Alfvén times. From that time onward, the value of the Hosking integral relative to that expected on dimensional grounds reaches a value of several thousand, a value that was also found earlier (Zhou *et al.* 2022).

Our present results have confirmed the existence of a resistively prolonged turbulent decay time whose value exceeds the Alfvén time by a factor $C_{\mathrm{M}} \approx \tau/\tau_{\mathrm{A}}$. As emphasized above, the fact that this ratio depends on the microphysical magnetic diffusivity is in principle surprising, because one of the hallmarks of turbulence is that its macroscopic properties should not depend on the microphysics of the turbulence. It would mean that it is not possible to predict this behavior of MHD turbulence by ignoring the microphysical magnetic diffusivity, as is usually done in so-called large eddy simulations.

The present results have shown that the decay time can exceed the Alfvén time by a factor of about, which is similar to what was found previously (Brandenburg *et al.* 2024). During intermediate times, however, the decay time can even be a hundred times longer than the Alfvén time. The dimensionless prefactors in the dimensionally motivated powerlaw expressions for length scale and mean magnetic energy density are also roughly similar to what was previously obtained from fully isotropic turbulence simulations.
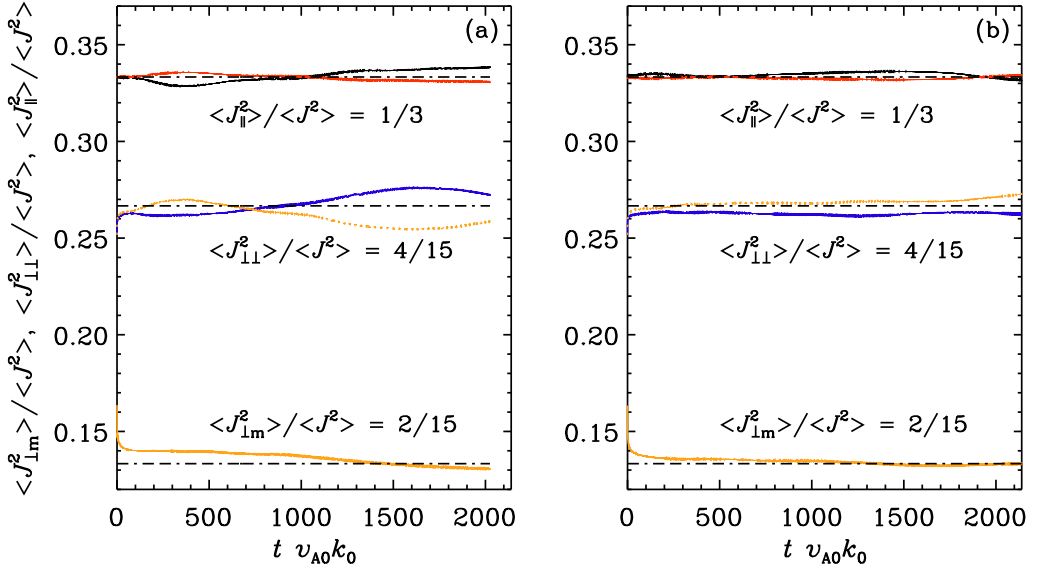
FIGURE 10. Evolution of $\langle \boldsymbol{J}_{\perp\mathrm{m}}^2 \rangle / \langle \boldsymbol{J}^2 \rangle$, $\langle \boldsymbol{J}_{\perp\perp}^2 \rangle / \langle \boldsymbol{J}^2 \rangle$, and $\langle \boldsymbol{J}_\parallel^2 \rangle / \langle \boldsymbol{J}^2 \rangle$ for decaying isotropic turbulence with an initial peak wavenumber $k_0/k_1 = 8$ using 1024^3 meshpoints (a) with helicity and (b) without helicity.

Declaration of Interests

The authors report no conflict of interest.

Data availability statement

The data that support the findings of this study are openly available on `http://norlx65.nordita.org/~brandenb/projects/Roberts-Decay/`. All calculations have been performed with the PENCIL CODE (Pencil Code Collaboration *et al.* 2021); DOI:10.5281/zenodo.3961647.

Authors' ORCIDs

A. Brandenburg, https://orcid.org/0000-0002-7304-021X
Longqing Yi, https://orcid.org/0000-0003-2378-5480
Xianshu Wu, https://orcid.org/0000-0003-3382-5132

Appendix A. $\langle \boldsymbol{J}_{\perp\perp}^2 \rangle / \langle \boldsymbol{J}^2 \rangle$ for isotropic turbulence

We have examined the evolution of $\langle \boldsymbol{J}_{\perp\perp}^2 \rangle / \langle \boldsymbol{J}^2 \rangle$ for isotropic turbulence using a setup similar to that of Brandenburg *et al.* (2023); see figure 10. The scale separation, i.e., the ratio of the peak wavenumber to the lowest wavenumber in the domain is 8 for this simulation and the Lundquist number, which is the rms Alfvén speed times the correlation length divided by the magnetic diffusivity, is about 10^4. The other parameters are as in the earlier work of Brandenburg *et al.* (2023); see the data availability statement of the present paper.
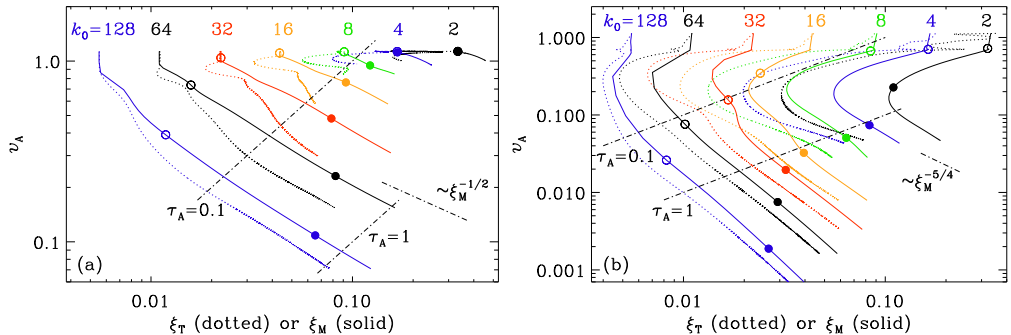
FIGURE 11. Same as figure 7(a), but for $c_\alpha = 3$, showing a parametric representation of B_{rms} versus $B_{\mathrm{rms}}/J_{\mathrm{rms}}$ and ξ_{M} for Roberts field I (left) with $k_0 = 2$ (black), 4 (blue), 8 (green), and 16 (orange), 32 (red), 64 (black), and 128 (blue). The open (filled) symbols in both plots indicate the times $t = 10$ ($t = 100$).

TABLE 3. Similar to table 1, showing normalized growth rates λ and peak times t_{p} for different values of k_0, but with the photon drag term included. Here, unlike the case of table 1, the values of B_0 are the same for Roberts fields I and II. The hyphen indicates that no growth occurred. The lowest value of k_0 has been set in italics to indicate that we used here what we called the rotated Roberts field.

field	$k_0 =$	*0.71*	1	2	4	8	16	32	64
I	$\lambda/v_{\mathrm{A0}}k_0 =$	—	—	0.01	0.02	0.05	0.05	0.05	0.05
II	$\lambda/v_{\mathrm{A0}}k_0 =$	0.12	0.15	0.19	0.20	0.22	0.22	0.19	0.13
I	$t_{\mathrm{p}}v_{\mathrm{A0}}k_0 =$	—	—	310	122	62	31	12	4.5
II	$t_{\mathrm{p}}v_{\mathrm{A0}}k_0 =$	78	51	27	14	6.7	3.5	1.8	1.2

Appendix B. Diagnostic diagrams for different k_0

In figure 7, we did already present a diagnostic diagrams of v_{A} vs. ξ_{M} for $k_{\mathrm{p}} = 16$. We also performed runs for different values of k_{p} to compute the growth rates and the times t_{p} of maximum growth in table 1, but not all the runs were long enough to compute similar tracks in the diagnostic diagram. In figure 11, we show such a diagram for a case in which a drag term of the form $-\alpha\boldsymbol{u}$ is included on the right-hand side of equation (2.6). Here, we choose a drag coefficient that automatically changes in time so as to allow for a nearly self-similar decay. Using a multiple of $1/t$ is an obvious possibility, but it would always be the same at all locations and for different types of flows. The local vorticity might be one possible option for a coefficient that varies in space and time, and has the right dimension. Another possibility, which is also the one chosen here, is to take α to be a multiple of $\sqrt{\mu_0/\rho_0}|\boldsymbol{J}|$ and write $\alpha = c_\alpha\sqrt{\mu_0/\rho_0}|\boldsymbol{J}|$, where c_α is a dimensionless prefactor, and $\mu_0 = \rho_0 = 1$ has been set. Again, as was already clear from figure 7, the tracks without helicity show a marked excursion to smaller values of ξ_{M} before displaying a decay of the form $v_{\mathrm{A}} \propto \xi_{\mathrm{M}}^{-\kappa}$. The corresponding values of $\lambda/v_{\mathrm{A0}}k_0$ and $t_{\mathrm{p}}v_{\mathrm{A0}}k_0$ are given in table 3.

Our definition of the Roberts fields follows the earlier work by Rheinhardt *et al.* (2014). In the original paper by Roberts (1972), however, the field was rotated by 45°. In that

case, $\phi = \cos k_0 x \mp \cos k_0 y$, where the upper and lower signs refer to Roberts fields I and II. For this field, a lower eigenvalue of the curl operator, namely $k_{\rm f} = k_0$, can be accessed. In that case, we can accommodated 1 pair of flux tubes instead of four. This can be done both for fields I and II. They are given by

$$\boldsymbol{B}_{\rm I} = \begin{pmatrix} \sin k_0 y \\ \sin k_0 x \\ \cos k_0 x - \cos k_0 y \end{pmatrix}, \quad \boldsymbol{B}_{\rm II} = \begin{pmatrix} \sin k_0 y \\ \sin k_0 x \\ \cos k_0 x + \cos k_0 y \end{pmatrix}, \qquad \text{(B 1)}$$

which satisfies $\boldsymbol{B}_{\rm I} \cdot \boldsymbol{\nabla} \times \boldsymbol{B}_{\rm I} = k_{\rm f} \boldsymbol{B}_{\rm I}^2$ and $\boldsymbol{B}_{\rm II} \cdot \boldsymbol{\nabla} \times \boldsymbol{B}_{\rm II} = 0$, just like the nonrotated field. But here, $k_{\rm f} = k_0$ is the eigenvalue of the curl operator.

REFERENCES

Armua, A., Berera, A. & Calderón-Figueroa, J. 2023 Parameter study of decaying magnetohydrodynamic turbulence. *Phys. Rev. E* **107** (5), 055206, arXiv: 2212.02418.

Banerjee, R. & Jedamzik, K. 2004 Evolution of cosmic magnetic fields: From the very early universe, to recombination, to the present. *Phys. Rev. D* **70**, 123003.

Biskamp, D. & Müller, W.-C. 1999 Decay Laws for Three-Dimensional Magnetohydrodynamic Turbulence. *Phys. Rev. Lett.* **83** (11), 2195–2198, arXiv: physics/9903028.

Brandenburg, A. & Banerjee, A. 2025 Turbulent magnetic decay controlled by two conserved quantities. *J. Plasma Phys.* **91** (1), E5, arXiv: 2406.11798.

Brandenburg, A. & Kahniashvili, T. 2017 Classes of Hydrodynamic and Magnetohydrodynamic Turbulent Decay. *Phys. Rev. Lett.* **118**, 055102, arXiv: 1607.01360.

Brandenburg, A., Kahniashvili, T. & Tevzadze, A. G. 2015 Nonhelical inverse transfer of a decaying turbulent magnetic field. *Phys. Rev. Lett.* **114** (7), 075001, arXiv: 1404.2238.

Brandenburg, A. & Larsson, G. 2023 Turbulence with Magnetic Helicity That Is Absent on Average. *Atmosphere* **14** (6), 932, arXiv: 2305.08769.

Brandenburg, A., Neronov, A. & Vazza, F. 2024 Resistively controlled primordial magnetic turbulence decay. *Astron. Astrophys.* **687**, A186, arXiv: 2401.08569.

Brandenburg, A., Sharma, R. & Vachaspati, T. 2023 Inverse cascading for initial magnetohydrodynamic turbulence spectra between Saffman and Batchelor. *J. Plasma Phys.* **89** (6), 905890606, arXiv: 2307.04602.

Brandenburg, A. & Subramanian, K. 2005 Astrophysical magnetic fields and nonlinear dynamo theory. *Phys. Rep.* **417**, 1–209, arXiv: astro-ph/0405052.

Frisch, U., Pouquet, A., Leorat, J. & Mazure, A. 1975 Possibility of an inverse cascade of magnetic helicity in magnetohydrodynamic turbulence. *J. Fluid Mech.* **68**, 769–778.

Hatori, T. 1984 Kolmogorov-Style Argument for the Decaying Homogeneous MHD Turbulence. *Phys. Soc. Jpn.* **53** (8), 2539.

Hosking, D. N. & Schekochihin, A. A. 2021 Reconnection-Controlled Decay of Magnetohydrodynamic Turbulence and the Role of Invariants. *Phys. Rev. X* **11** (4), 041005, arXiv: 2012.01393.

Hosking, D. N. & Schekochihin, A. A. 2023 Cosmic-void observations reconciled with primordial magnetogenesis. *Nat. Comm.* **14**, 7523, arXiv: 2203.03573.

Jiang, K., Pukhov, A. & Zhou, C. T. 2021 Magnetic field amplification to gigagauss scale via hydrodynamic flows and dynamos driven by femtosecond lasers. *New J. Phys.* **23** (6), 063054, arXiv: 2006.03326.

Pencil Code Collaboration, Brandenburg, A., Johansen, A., Bourdin, P., Dobler, W., Lyra, W., Rheinhardt, M., Bingert, S., Haugen, N., Mee, A., Gent, F., Babkovskaia, N., Yang, C.-C., Heinemann, T., Dintrans, B., Mitra, D., Candelaresi, S., Warnecke, J., Käpylä, P., Schreiber, A., Chatterjee, P., Käpylä, M., Li, X.-Y., Krüger, J., Aarnes, J., Sarson, G., Oishi, J., Schober, J., Plasson, R., Sandin, C., Karchniwy, E., Rodrigues, L., Hubbard, A., Guerrero, G., Snodin, A., Losada, I., Pekkilä, J. & Qian, C. 2021 The Pencil Code, a modular MPI code for partial differential equations and particles: multipurpose and multiuser-maintained. *J. Open Source Softw.* **6** (58), 2807.

Rheinhardt, M., Devlen, E., Rädler, K.-H. & Brandenburg, A. 2014 Mean-field dynamo

action from delayed transport. *Mon. Not. Roy. Astron. Soc.* **441**, 116–126, arXiv: 1401.5026.

ROBERTS, G. O. 1972 Dynamo Action of Fluid Motions with Two-Dimensional Periodicity. *Phil. Trans. Roy. Soc. Lond. Ser. A* **271** (1216), 411–454.

TZEFERACOS, P., RIGBY, A., BOTT, A. F. A., BELL, A. R., BINGHAM, R., CASNER, A., CATTANEO, F., CHURAZOV, E. M., EMIG, J., FIUZA, F., FOREST, C. B., FOSTER, J., GRAZIANI, C., KATZ, J., KOENIG, M., LI, C. K., MEINECKE, J., PETRASSO, R., PARK, H. S., REMINGTON, B. A., ROSS, J. S., RYU, D., RYUTOV, D., WHITE, T. G., REVILLE, B., MINIATI, F., SCHEKOCHIHIN, A. A., LAMB, D. Q., FROULA, D. H. & GREGORI, G. 2018 Laboratory evidence of dynamo amplification of magnetic fields in a turbulent plasma. *Nat. Comm.* **9**, 591, arXiv: 1702.03016.

VACHASPATI, T. 2021 Progress on cosmological magnetic fields. *Reports on Progress in Physics* **84** (7), 074901, arXiv: 2010.10525.

ZHOU, H., SHARMA, R. & BRANDENBURG, A. 2022 Scaling of the Hosking integral in decaying magnetically dominated turbulence. *J. Plasma Phys.* **88** (6), 905880602, arXiv: 2206.07513.